Journal of Materials Chemistry A

ROYAL SOCIETY OF CHEMISTRY

PAPER

View Article Online
View Journal | View Issue

Cite this: J. Mater. Chem. A, 2022, 10, 10201

Enhanced cathode integrity for zinc–manganese oxide fiber batteries by a durable protective layer†

Jiawei Wang,‡ Meng Liao,‡ Xinlin Huang, Pengzhou Li, Jiaxin Li, Lei Ye, Yue Gao, Huisheng Peng and Bingjie Wang *

Received 6th February 2022
Accepted 2nd April 2022

DOI: 10.1039/d2ta00982j

rsc.li/materials-a

Aqueous fiber batteries with high safety and flexibility have attracted extensive attention for their promising applications in next-generation wearable electronics. However, the further applications of aqueous fiber batteries are severely hindered by mechanical instability and insufficient electrochemical performance. Here, a durable protective layer with a compact structure and high conductivity is designed to endow the fiber cathode with improved integrity and reaction kinetics. The resulting Zn–MnO_2 fiber battery demonstrates high durability and stable energy output under varying deformations and delivers a long-term cycle life of up to 4000 cycles at 2 A g^{-1}. It also shows a high specific capacity of 332 mA h g^{-1} and an improved rate capability of 163 mA h g^{-1} at 5 A g^{-1}. The design of the durable protective layer provides a useful strategy for the construction of fiber batteries with high stability and performance.

Introduction

Wearable electronics in close contact with skin call for highly safe and flexible power solutions.[1–4] In this regard, aqueous Zn-ion batteries (AZIBs) have attracted increasing interest due to a low redox potential of −0.76 V *vs.* the standard hydrogen electrode (SHE), a high theoretical specific capacity of 820 mA h g^{-1}, and low cost of the Zn anode.[5–9] As a promising paradigm, aqueous Zn–MnO_2 batteries with $ZnSO_4$/$MnSO_4$ electrolytes demonstrate broad electrochemical windows, eco-friendliness, high specific capacity, and facile fabrication. Incorporating aqueous Zn–MnO_2 fiber batteries into breathable battery textiles provides an efficient and safe solution for powering wearable electronics.[10–15]

However, the promising MnO_2 cathode still suffers from inferior conductivity, which leads to sluggish kinetics and poor rate capability, hindering its further applications in quick charging electronics.[16–18] In addition, MnO_2 cathode materials are commonly troubled by dissolution due to the disproportionation of Mn element upon cycling and thus the rapid capacity decay.[19] In response, electrolytes with $MnSO_4$ additives are widely used to suppress Mn dissolution in Zn–MnO_2 batteries.[20] This strategy is effective in decreasing the dissolution of microscopic quantities of MnO_2 while it cannot prevent the peeling off of bulky MnO_2 precipitates, which is inevitable during the deformation of flexible batteries and often results in more severe capacity loss. As a result, developing a strategy to improve the electrochemical performance and stabilize the MnO_2 cathode at multiple scales at the same time is desirable but highly challenging. Protection through fixing surface materials may be inspired by the strategy of preventing landslides. When controlling debris flow and preventing soil erosion, a net will be used to cover the surface of the mountain to prevent large stones from falling off, and then vegetation will be planted in the gaps of the net to further maintain the integrity of the land and prevent the loss of small amounts of soil, so the landscape will be perfectly protected at multiple scales.

Herein, like the protection from landslides, a durable protective layer was developed to stabilize the incorporated cathode materials at both macroscopic and microscopic scales for flexible aqueous Zn–MnO_2 fiber batteries with high integrity and durability. In this strategy, the aligned CNT film was wrapped on the MnO_2 fiber cathode to enhance mechanical integrity due to the high mechanical strength inherited from the alignment structure, decreasing the loss of bulky MnO_2 particles at the macroscopic scale under deformations. PEDOT, as a typical conductive polymer, was further introduced to filter the micro-voids between the aligned CNT film and MnO_2, forming a robust, hierarchical protective layer to reduce the loss of active materials. Mediated by the incorporation of this multifunctional protective layer, the resulting aqueous Zn–MnO_2 fiber battery maintained a stable structure under bending and a long-time cycle test, delivering a high cycling stability with 90% capacity retention after 4000 charge/discharge cycles at 2 A g^{-1}. Meanwhile, the high conductivity of the aligned CNT and PEDOT layers enhanced the overall electrical conductivity of the fiber cathode, resulting in improved rate capability with

Laboratory of Advanced Materials, State Key Laboratory of Molecular Engineering of Polymers, Department of Macromolecular Science, Fudan University, Shanghai 200438, China. E-mail: wangbingjie@fudan.edu.cn

† Electronic supplementary information (ESI) available. See https://doi.org/10.1039/d2ta00982j

‡ Equally contributing authors.

a decent specific capacity of 163 mA h g^{-1} even at 5 A g^{-1}. These results demonstrate that the design of the protective layer provides a promising strategy to realize aqueous Zn-ion fiber batteries with both high mechanical stability and electrochemical performance.

Results and discussion

Morphology and structure of the fiber cathode with the durable protective layer

The design and fabrication of the durable protective layer are schematically shown in Fig. 1a, S1 and S2.† The fiber cathode was first prepared by electrodepositing MnO_2 nanoparticles onto a porous current collector with high specific surface area (Fig. S3†) in a multi-strand assembled manner (Fig. S4†) (denoted as CM, Fig. 1b and c and S5†). The obtained CM was then wrapped by an ultra-thin layer of aligned CNT film to produce the CNT/MnO_2 hybrid fiber cathode (denoted as CMC, Fig. 1d and e). The wrapping process is further shown in Fig. S1b† and the CNT film with good alignment is expected to provide effective protection and facilitate electron transportation during the charge/discharge process. Following that, a thin layer of conductive PEDOT was synthesized on the CMC to infiltrate the micro-channels existing on the outer aligned CNT scaffold (denoted as CMCP, Fig. 1f and g), which was supposed to further enhance the durability of the protective layer and the electrical conductivity of the fiber cathode. Note that other conductive polymers could also play the functional roles like PEDOT adopted in this work.[21,22] The pores and hydrophilic features of the durable protective layer on the CMCP are reserved for the infiltration of aqueous electrolyte (Fig. 1g and S6†).

The construction of a durable protective layer on the MnO_2 fiber cathode was first validated by SEM-EDS analysis, showing a homogeneous distribution of both Mn and S elements (Fig. S7†). The interfaces in CMCP were then dissected by the cross-sectional image captured through FIB technology (Fig. 1h and S8†). As expected, the cathode materials (MnO_2 nanoparticles) were effectively sealed by the durable protective layer (CNT/PEDOT hybrid thin film), ensuring the stable integrity of CMCP under both mechanical and electrochemical variations. This interfacial stability in CMCP was then revealed by TEM and HRTEM analysis (Fig. 1i). Consistent with the SEM results, clear lattice fringes with a spacing of 0.38 nm attributed to the (002)

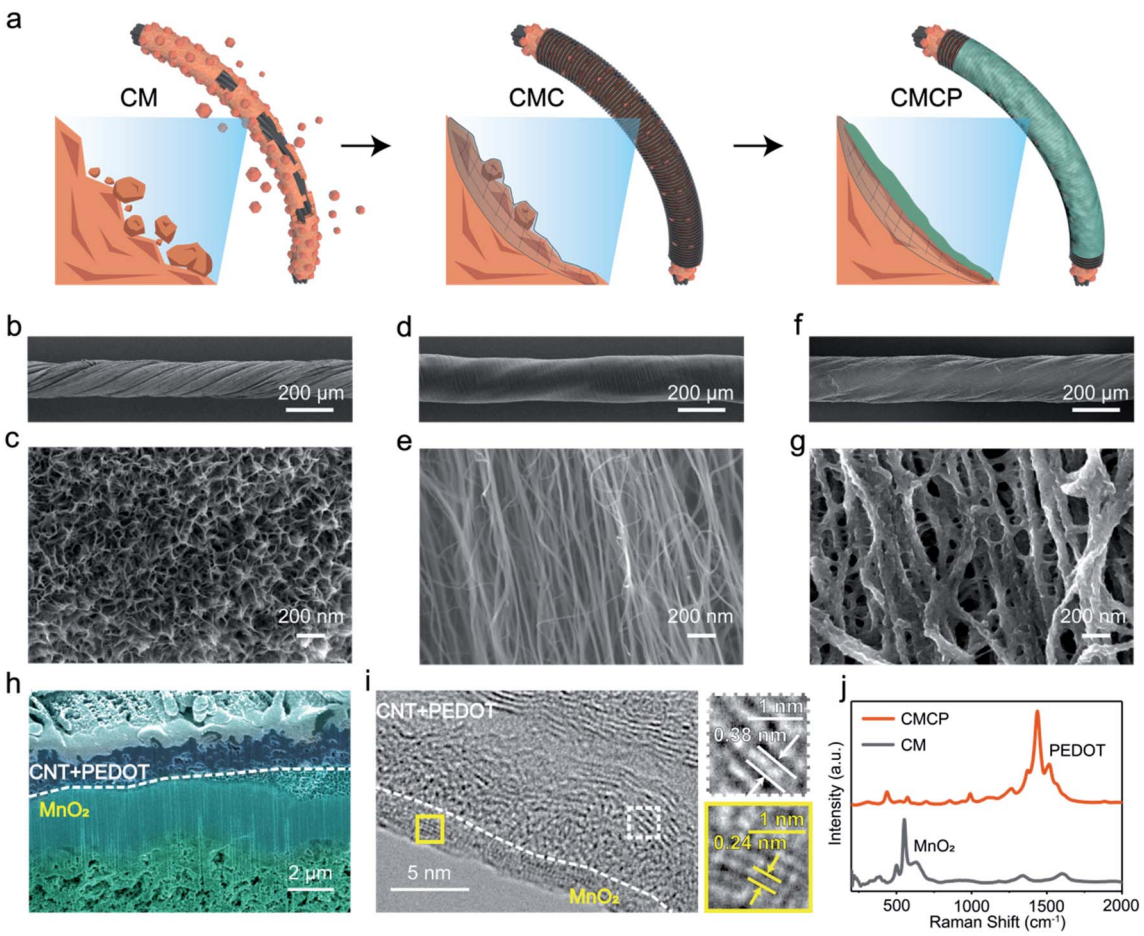

Fig. 1 (a) Schematic illustration of the structure and details of CM, CMC, and CMCP, respectively. (b and c) SEM images of CM at low and high magnifications, respectively. (d and e) SEM images of CMC at low and high magnifications, respectively. (f and g) SEM images of CMCP at low and high magnifications, respectively. (h) SEM image of the cross section of CMCP. (i) HRTEM images of CMCP. (j) Raman spectra of CM and CMCP.

plane of graphite carbon (JCPDS no. 75-1621) and 0.24 nm attributed to the (311) plane of MnO_2 (JCPDS no. 44-0992) were determined (Fig. 1i, right panels).[23]

Spectroscopy characterization was further used to explore the chemical evolution of the modified MnO_2 fiber cathode. Initially in the Raman spectrum of CM, three characteristic Mn–O stretching vibrations of the [MnO_6] group from MnO_2 appeared at 501, 553, and 633 cm^{-1} (Fig. 1j).[24] Upon the incorporation of a multifunctional layer containing PEDOT to form CMCP, the above characteristic peaks from MnO_2 became weakened, with a new emerging peak at ~1500 cm^{-1}, which was in good agreement with the PEDOT peak. XPS spectra in Fig. S9† demonstrated the distinct Mn signals of CM and S of the CMCP sample, again indicating the formation of the MnO_2 and PEDOT layer, and the absence of Mn signals of CMCP indicated the compact structure of the CNT/PEDOT layer. Fig. S10† displays three similar XRD patterns of the prepared cathodes, in which most diffraction peaks could be indexed to λ-MnO_2 (JCPDS no. 44-0992) except for a peak located at 25.5° coming from CNTs in the current collector.[25] This result confirmed that the introduction of a multifunctional protective layer had little effect on the structure of electrodeposited MnO_2.

Mechanical stability of the MnO_2 cathode with the durable protective layer

The durability against deformations is essential for flexible batteries.[26,27] The mechanical instability of the MnO_2 cathode was reflected in two aspects: one is the exfoliation of bulky particles in the bending process, and the other is the dissolution of Mn^{2+} during cycling. For the first type, aligned CNT films were employed in the construction of the CMC cathode to prevent the exfoliation of MnO_2 particles. The comparison of bent CM and CMC cathodes is shown in Fig. 2a–f. Due to the intrinsic brittleness of MnO_2, obvious cracks appeared at the bending point of the CM sample under a 180° bending angle, yielding the peeling off of bulky MnO_2 (Fig. 2a). In contrast, no crack was identified in the CMC sample protected by the aligned CNTs (Fig. 2b and c). This effectiveness of protection by the aligned CNT layer was further proved by bending the fiber cathodes under a different bending angle (90°) and after repeating the bending cycles (Fig. S11†). Furthermore, an ultrasonic vibration experiment was carried out to simulate the state of the fiber battery under high-frequency mechanical disturbance to prove the protective effect of the CNT film on bulky MnO_2 (Fig. S12†). Fig. S12a† shows that CM and CMC were placed in centrifuge tubes filled with clear deionized water. After 5 min ultrasonic vibration treatment, the CM sample turned turbid and there was sediment at the bottom, while the CMCP sample remained clear (Fig. S12b†). Then an equal amount of acidified aniline monomer was added into the two centrifuge tubes (Fig. S12c†) because MnO_2 can initiate the polymerization of the transparent aniline monomer into green polyaniline under acidic conditions.[22] The CM sample distinctly turned green while CMCP remained transparent, demonstrating that the CNT film can promote the mechanical integrity of the fiber cathode even under extreme mechanical interference and prevent bulky MnO_2 from shedding. This could also be confirmed by the element analysis of dissolved Mn after an ultrasonic vibration experiment test (Fig. S13†). The morphology of the fiber cathodes after the ultrasonic vibration test is shown in Fig. 2d and e. Without the protection of the CNT film, bulky MnO_2 was exfoliated from the current collector (Fig. 2d), while the CNT film after the ultrasonic vibration test retained a flat surface although there were small gaps (Fig. 2e). Especially at high magnification, it was observed that the CNT bundles still maintained a certain orientation and could continue to be a protective layer (Fig. 2f). The CNT film can not only protect MnO_2 mechanically but also relieve the stress of the MnO_2 layer to a certain extent. As schematically shown in Fig. 2g and S14,† once bent, intensified and aggregated internal stress of the active material was observed in the CM fiber cathode.[28] This would further result in the falling off of MnO_2 from the unprotected fiber cathode as the capacity decayed under deformations. In contrast, once the fiber electrode was protected by aligned CNT film with high mechanical strength, the corresponding internal stress upon bending was decreased, which could avoid the occurrence of cracking as well as the exfoliation of the protected MnO_2 layer.

In the second place, the PEDOT layer was further employed to densify the CNT film, in order to restrain the dissolution of small particles of MnO_2 or Mn^{2+}. The efficient protection effect was revealed by inductively coupled plasma optical emission spectrometry (ICP-OES) analysis. Upon increasing the number of bending cycles, the amount of exfoliated Mn element in the aqueous electrolyte from the CMCP cathode was kept at a low value of ~0.2 μg, suggesting the effective protection of the CNT/PEDOT protective layer (Fig. 2h). In contrast, the amount of exfoliated Mn element from the CM fiber cathode showed an increasing tendency with the increasing bending cycles, and a total mass of >10 μg was finally determined. As such, the protective effect was also found in the galvanostatic charge/discharge processes. With the protective layer, even after galvanostatic cycling at high depth (at 0.2 A g^{-1}), there was negligible Mn dissolution in the Zn-CMCP fiber battery, while the Zn-CM battery showed severe Mn dissolution of up to >30 μg (Fig. 2i). Besides, the CMCP fiber cathode also demonstrated much enhanced tensile breaking strength and breaking strain over other fiber cathodes (Fig. S15†). Collectively, the introduction of the durable protective layer effectively reduced the undesirable structural instabilities under deformations as well as the dissolution of active materials upon recurring charge/discharge processes, offering the possibility for a high-performance fiber cathode with decent durability.

Electrochemical properties of the fabricated Zn–MnO_2 batteries

Apart from the mechanical enhancements, the incorporation of the durable protective layer also contributed to an improved electrochemical performance for the aqueous Zn–MnO_2 fiber battery. To probe the role of the durable protective layer in Zn^{2+} storage/release processes, the CM, CMC, and CMCP cathode fibers were first paired with a Zn-coated fiber (Fig. S16 and S17†)

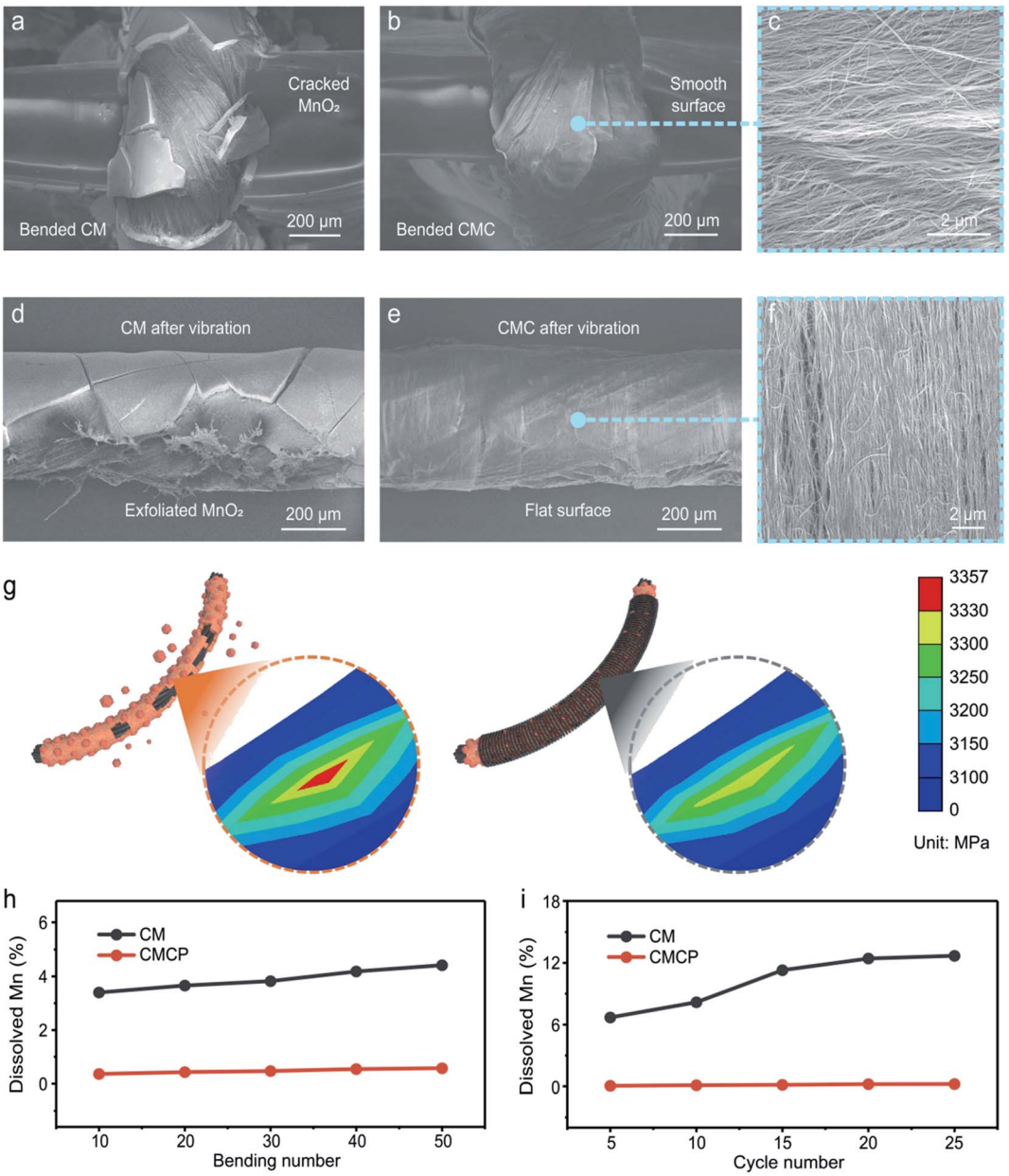

Fig. 2 (a and b) SEM images of CM and CMC under bending deformation at low magnification. (c) SEM image of CNT film under bending deformation at high magnification. (d and e) SEM images of CM and CMC after a vibration test at low magnification. (f) SEM image of CNT film after a vibration test at high magnification. (g) Finite element analysis (FEA) of the stress distribution of CM and CMC under bending. (h and i) Element analysis of Mn in 2 M $ZnSO_4$ aqueous electrolyte of CM and CMCP after bending and cycling.

in 2 M $ZnSO_4$ and 0.2 M $MnSO_4$ aqueous electrolyte to form an AZIB. The fiber cathode with PEDOT directly deposited on the MnO_2 (denoted as CMP) was also fabricated, in order to explore the synergistic effect of the two components in the protective layer. Fig. 3a compares typical CV curves at 0.2 mV s^{-1}. As is depicted, the introduction of the aligned CNT or PEDOT layer could afford enhanced peak current density, indicating facilitated reaction kinetics compared to that of the CM fiber cathode. The offset of the reduction peak in the CMP sample originated from the dense morphology of PEDOT (Fig. S18†), preventing the direct contact of the electrolyte with MnO_2 and impeding the intercalation of ions. Meanwhile, the CNT scaffold provided voids for the protective layer, so a synergetic enhancement was further observed in the Zn-CMCP battery with the protection of a durable protective layer concurrently containing aligned CNT and PEDOT layers (Fig. 3b). This significant enhancement in kinetics was further revealed by the discharge curves at 100 mA g^{-1} (Fig. 3c). The Zn-CMCP battery exhibited two significantly prolonged discharge plateaus at an average voltage of ~1.4 V with a high specific capacity of 332 mA h g^{-1} demonstrating the facilitated reaction kinetics of the durable protective layer. The charge storage contribution of

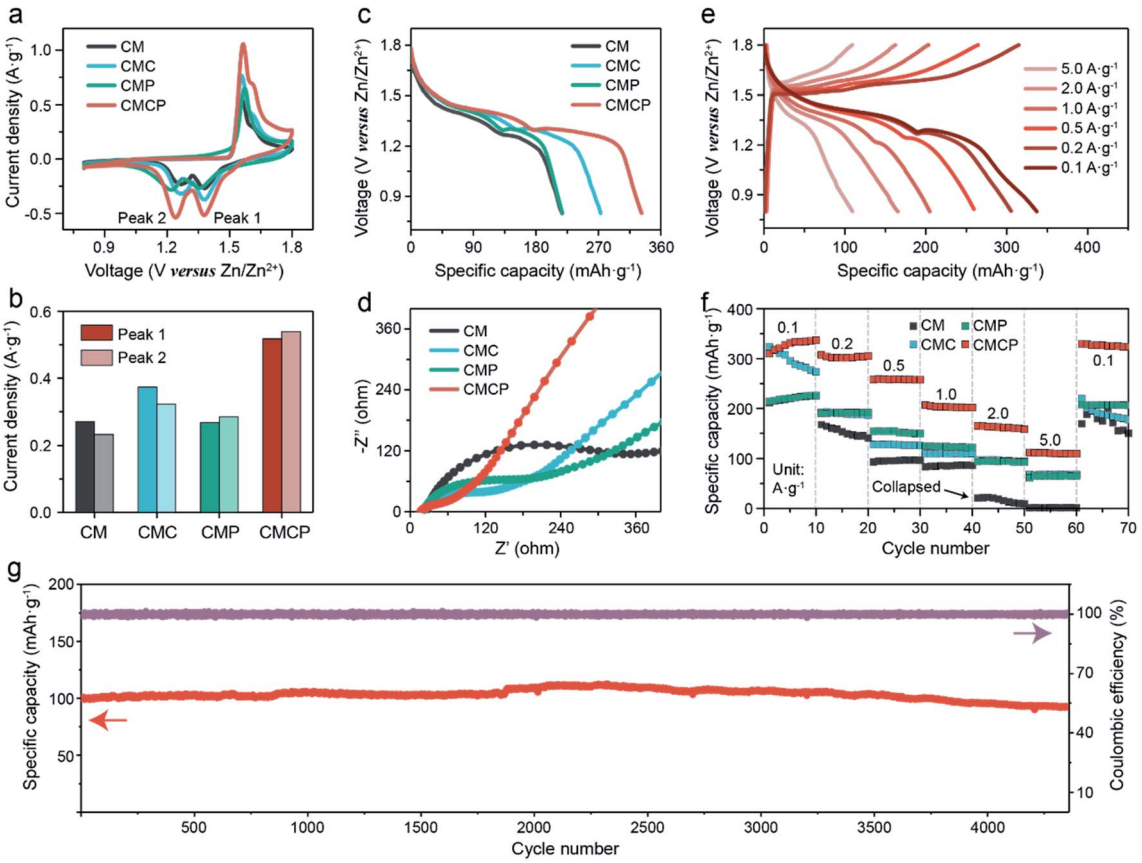

Fig. 3 Electrochemical performance of Zn-CM, CMC, CMP, and CMCP batteries. (a) CV curves at 0.2 mV s^{-1}. (b) Comparison of discharge peak current densities obtained from (a). (c) Galvanostatic discharge curves at 0.1 A g^{-1}. (d) Nyquist plots at open-circuit voltages. (e) Galvanostatic discharge profiles of the Zn-CMCP battery at increasing current densities from 0.1 to 5 A g^{-1}. (f) Rate capability. (g) Cycling performance of the Zn-CMCP battery at 2 A g^{-1} and the corresponding CE.

the aligned CNT and PEDOT layers was measured to be negligible (Fig. S19†) and the additional capacity was attributed to the higher utilization and electrical conductivity of the active material.

Fig. 3d shows the charge transfer resistance (R_{ct}) of the assembled battery which followed the order Zn-CMCP < CMC < CMP < CM, demonstrating the effectively facilitated ionic motion of the CMCP cathode. The protective layer with 3D ion channels afforded more favorable electrode/electrolyte interfaces for Zn^{2+} and charge transfer, and delivered marked high specific capacities of 337, 305, 259, 205, and 165 mA h g^{-1} upon increasing applied current densities from 0.1 to 5 A g^{-1} (Fig. 3e). The rate capability of the Zn-CMCP battery was further revealed by comparing with those based on its CM, CMC, and CMP counterparts upon varying the current density from 0.1 to 5 A g^{-1} (Fig. 3f). The capacity of the Zn-CMCP battery could immediately recover within the reversal of the applied current density while the other three counterparts demonstrated much lower capacities at each rate. Apart from the enhanced rate capability, the introduction of a durable protective layer also contributed to improved cycling stability of the resulting AZIB fiber. As shown in Fig. 3g, the Zn-CMCP battery achieved a capacity retention of >90% over 4000 cycles with coulombic efficiency (CE) of ~100% at a representative current density of 2 A g^{-1}. The slight increase appearing within 2000–2500 cycles was due to the temperature increment during the long-term test. It also demonstrated outstanding cycling performance at other current densities of 1 and 0.5 A g^{-1} (Fig. S20 and S21†). The surface morphology of the cycled CMCP electrode was retained after cycling, indicating the structural stability of the durable protection layer (Fig. S22†). The facilitated kinetics of the Zn-CMCP battery was then further revealed by the CV study (ESI 2, Fig. S23 and S24†), validating the improved kinetics and high surface reactivity.

Mechanical and electrochemical stability under various deformations

In view of the high mechanical stability and impressive electrochemical capability, the Zn-CMCP fiber battery was expected to maintain stability and high performance in practical application. Based on the application scenario of a fiber battery, a series of tests of fiber batteries under dynamic deformations were conducted. Benefiting from the durable protective layer, the Zn-CMCP fiber battery remained almost unchanged in the corresponding discharge curves under varying deformations including twisting and folding (Fig. 4a). The Zn-CMCP fiber

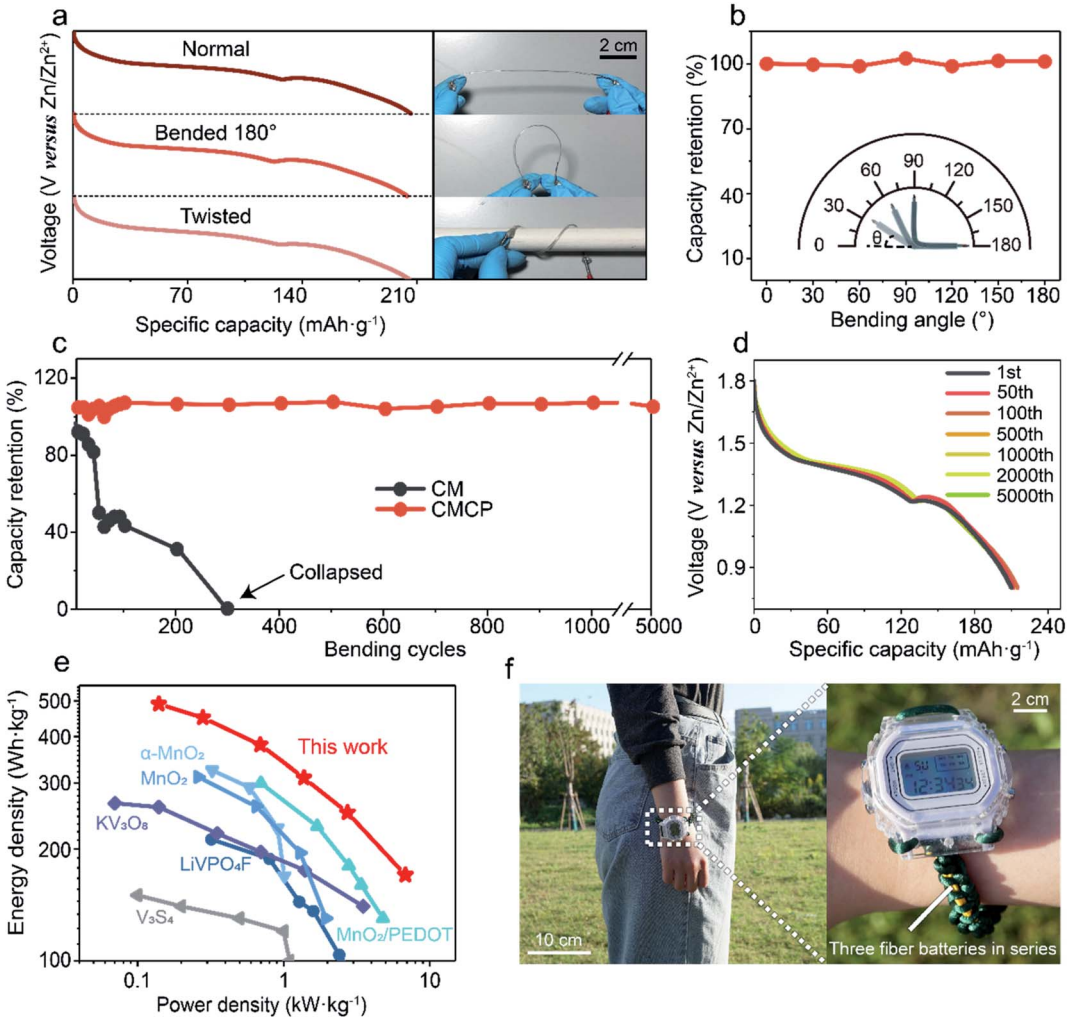

Fig. 4 (a) Galvanostatic discharge curves of the Zn-CMCP fiber battery under varying deformations (1 A g^{-1}). (b) Dependence of capacity retention of the Zn-CMCP fiber battery with increasing device bending angle from 0 to 180°. (c) Comparison of capacity retention between Zn-CM and CMCP fiber batteries with increasing bending cycles. (d) Galvanostatic discharge curves of the Zn-CMCP fiber battery (1 A g^{-1}) with increasing bending cycles. (e) Ragone plot comparison with some reported flexible aqueous ZIBs. (f) Photograph of an electronic watch powered by three Zn-CMCP fiber batteries in series.

battery also exhibited a stable output of ~1.5 V under constant deformations (Fig. S25†). This stability was then revealed by an electronic timer powered by a fiber battery against deformations (Fig. S26†). Furthermore, the capacity retention of the fiber battery could be well maintained at >90% under different bending angles (Fig. 4b) and bending cycles (180°, 5000 cycles, Fig. 4c and S27†). In stark contrast, the fiber battery based on the unprotected MnO_2 cathode suffered a rapid capacity decay (capacity retention <10%) even in the first 100 bending cycles. The protected CMCP-based fiber battery could still afford highly overlapped discharge curves, even after more than 5000 bending cycles, further illustrating the improved durability from the durable protective layer (Fig. 4d). In contrast, the output voltage and specific capacity of the Zn-CM fiber battery gradually decreased with the increase of bending cycles (Fig. S28†).

The Zn-CMCP fiber battery demonstrated an energy density up to 490 W h kg^{-1} at a power density of 0.14 kW kg^{-1}, outperforming those of previously reported flexible AZIBs as shown in the Ragone plots (Fig. 4e).[29–34] The Zn-CMCP fiber batteries could be water-proof (Fig. S29†) and connected in parallel or in series (Fig. S30 and S31†) to meet varying requirements upon applications. As a demonstration, Zn-CMCP fiber batteries were woven into a flexible and breathable power strip to light an electronic watch (Fig. 4f), showing decorative and energy-supply functions at the same time.

Conclusion

In summary, we have designed a durable protective layer to effectively protect the fiber cathode and endow higher electrical conductivity, thus enabling the fabrication of flexible aqueous Zn-ion fiber batteries with both high mechanical durability and electrochemical performance. Benefiting from the synergistic effect of the aligned CNT film and PEDOT layer, high durability under varying deformations was demonstrated and the

fabricated Zn-CMCP fiber battery achieved 100% capacity retention under 5000 bending cycles and a cycle life of up to 4000 cycles at 2 A g^{-1}. It also delivered a high specific capacity of 332 mA h g^{-1} and a high rate capability of 163 mA h g^{-1} at 5 A g^{-1}. This design could attract intense interest and have great potential for the construction of aqueous fiber batteries with both high mechanical stability and electrochemical performance.

Methods

Preparation of the current collector of the fiber battery

The fiber current collector was made of floating CNT fibers synthesized by floating catalyst chemical vapor deposition with thiophene (1–2 wt%)/ferrocene (1–2 wt%) as the catalyst, and flowing ethanol (>97 wt%) as a carbon source, Ar (200 sccm) as carrier gas, and H_2 (2000 sccm) as reduction gas.[35] In this work, the flexible current collectors were made with multi-strand CNTs with diameters of ~200 μm as shown in Fig. S4† with specific clarification.

Preparation of the MnO_2/current collector cathode (CM)

The fiber electrode of CM was prepared by electrodepositing nano-structured MnO_2 onto the above CNT fiber substrate. The electrodeposition was conducted in a solution containing $Mn(Ac)_2$ (0.1 M) and Na_2SO_4 (0.1 M) at room temperature with Pt as the counter electrode and a Ag/AgCl electrode as the reference electrode. The pulse electrodeposition mode (1.5 V for 1 s and 0.7 V for 10 s) was applied and MnO_2 was formed through the following reaction, *i.e.*, $Mn^{2+} + 2H_2O \rightarrow MnO_2 + 4H^+ + 2e^-$. The obtained sample was washed with deionized water and dried in the air. The mass loading of MnO_2 was measured to be ~1 mg cm^{-1} with an electronic macro-balance (BT25S, 0.0001 mg).

Preparation of the CNT/MnO_2/current collector cathode (CMC)

A spinnable CNT array with a width of 1 cm was synthesized by chemical vapor deposition with Fe (1.2 nm in thickness)/Al_2O_3 (3 nm in thickness) as the catalyst on a Si substrate. Flowing ethylene (90 sccm), Ar (400 sccm), and H_2 (30 sccm) were used as the carbon source, carrier gas, and reduction gas, respectively. The reaction was carried out in a CVD furnace at 740 °C for 10 min. The two ends of the CM fiber were fixed by two clamps connected with motors and the spinnable CNT array was fixed onto a precisely motorized translation stage. A continuously aligned CNT sheet film (~18 nm in thickness and 1 cm in width) was drawn out of the spinnable CNT array and then wrapped onto the CM fiber at an angle of 20°. The wound aligned CNT sheet evenly covered the whole CM fiber (Fig. S1b†).

Preparation of the PEDOT/CNT/MnO_2/current-collector cathode (CMCP)

The fiber electrode of CMCP was synthesized by electrodepositing PEDOT onto the CMC fiber in an aqueous solution of 3,4-ethylenedioxythiophene (EDOT) (0.03 M), lithium perchlorate (0.10 M), and sodium dodecyl sulfate (0.07 M). A potential of 1.0 V *vs.* SCE was applied for 10 s.

Preparation of the PEDOT/MnO_2/current-collector cathode (CMP)

For comparison, the CMP electrode was synthesized on the CM sample by electrodeposition at 1.0 V *vs.* SCE in a solution of EDOT (0.03 M), lithium perchlorate (0.1 M), and sodium dodecyl sulfate (0.07 M).

Synthesis of the flexible Zn anode

A flexible Zn fiber anode was prepared by a facile electrodeposition method. Electroplating was performed in a solution of $ZnSO_4$ (1 M) and KCl (1 M) at −0.8 V *vs.* Zn rod for 1000 s, then the metallic zinc was deposited on the current collector. The obtained fiber anode was washed with deionized water and dried under vacuum at room temperature.

Assembly of the fiber Zn–MnO_2 full battery

Zn–MnO_2 fiber batteries were assembled by pairing the CM, CMC, CMP, or CMCP fiber cathodes with a fiber Zn anode in 1 mL electrolyte of $ZnSO_4$ (2.0 M) and $MnSO_4$ (0.2 M) aqueous solution, followed by packing with a commercial EVA heat shrink tube. The two ends of the fiber battery were sealed with UV curing adhesive and small sections of electrodes were exposed outside the package to connect the wire.

Materials characterization

The compositions and morphologies of the fiber current collector, CM, CMC, CMCP, CMP, and fiber Zn anode electrodes were characterized by scanning electron microscopy (Zeiss FE-SEM Ultra 55 operated at 5 kV), transmission electron microscopy (JEOL JEM-2100F operated at 200 kV), energy dispersive spectroscopy, Raman spectroscopy (Dilor LabRam-1B, He–Ne laser of 4 mW, excitation wavelength of 532 nm), X-ray diffraction (Rigaku Ultima IV powder X-ray diffractometer with Cu Kα radiation), and X-ray photoelectron spectroscopy (Thermo Scientific K-Alpha). Photographs were taken using a camera (SONY A6000, Japan). The bending experiments of fiber batteries were performed using a home-made step motor with a bending radius of 3 mm.

Electrochemical measurements

Galvanostatic charge/discharge measurements were conducted using a LAND electrochemical station (CT2001A-5V5mA8CT). The current density and specific capacity were normalized based on the mass of the synthesized MnO_2 in each cathode electrode. CV and electrochemical impedance spectroscopy (EIS) tests were performed on a CHI660E electrochemical workstation. EIS was conducted with an AC voltage of 5 mV amplitude at the frequency range of 100 kHz to 10 mHz.

Conflicts of interest

The authors declare no conflict of interest.

Acknowledgements

This work was supported by STCSM (20JC1414902, 21511104900) and SHMEC (2017-01-07-00-07-E00062).

References

1 R. Li, L. Li, R. Jia, K. Jiang, G. Z. Shen and D. Chen, *Small Methods*, 2020, **4**, 2000363.
2 M. Liao, J. Wang, L. Ye, H. Sun, P. Li, C. Wang, C. Tang, X. Cheng, B. Wang and H. Peng, *J. Mater. Chem. A*, 2021, **9**, 6811–6818.
3 F. Mo, G. Liang, Z. Huang, H. Li, D. Wang and C. Zhi, *Adv. Mater.*, 2020, **32**, 1902151.
4 J. He, C. Lu, H. Jiang, F. Han, X. Shi, J. Wu, L. Wang, T. Chen, J. Wang, Y. Zhang, H. Yang, G. Zhang, X. Sun, B. Wang, P. Chen, Y. Wang, Y. Xia and H. Peng, *Nature*, 2021, **597**, 57–63.
5 M. Liao, J. Wang, L. Ye, H. Sun, Y. Wen, C. Wang, X. Sun, B. Wang and H. Peng, *Angew. Chem., Int. Ed.*, 2020, **59**, 2273–2278.
6 J. Ding, Z. Du, B. Li, L. Wang, S. Wang, Y. Gong and S. Yang, *Adv. Mater.*, 2019, **31**, e1904369.
7 R. Wang, M. Yao, S. Huang, J. Tian and Z. Niu, *Adv. Funct. Mater.*, 2021, **31**, 2009209.
8 G. Fang, S. Liang, Z. Chen, P. Cui, X. Zheng, A. Pan, B. Lu, X. Lu and J. Zhou, *Adv. Funct. Mater.*, 2019, **29**, 1905267.
9 Y. Tong, X. Li, S. Su, J. Li, J. Fang, B. Liang, J. Hou and M. Luo, *J. Colloid Interface Sci.*, 2022, **606**, 645–653.
10 Y. Jin, L. Zou, L. Liu, M. H. Engelhard, R. L. Patel, Z. Nie, K. S. Han, Y. Shao, C. Wang, J. Zhu, H. Pan and J. Liu, *Adv. Mater.*, 2019, **31**, e1900567.
11 T. N. Nguyen, B. Iranpour, E. Cheng and J. D. W. Madden, *Adv. Energy Mater.*, 2021, **12**, 2103148.
12 X. Shen, X. Wang, Y. Zhou, Y. Shi, L. Zhao, H. Jin, J. Di and Q. Li, *Adv. Funct. Mater.*, 2021, **31**, 2101579.
13 W. Sun, F. Wang, S. Hou, C. Yang, X. Fan, Z. Ma, T. Gao, F. Han, R. Hu, M. Zhu and C. Wang, *J. Am. Chem. Soc.*, 2017, **139**, 9775–9778.
14 Z. Liu, Y. Yang, S. Liang, B. Lu and J. Zhou, *Small Structures*, 2021, **2**, 2100119.
15 X. Xie, H. Fu, Y. Fang, B. Lu, J. Zhou and S. Liang, *Adv. Energy Mater.*, 2021, **12**, 2102393.
16 Y. Hu, Y. Wu and J. Wang, *Adv. Mater.*, 2018, **30**, e1802569.
17 T. Zhang, Y. Tang, G. Fang, C. Zhang, H. Zhang, X. Guo, X. Cao, J. Zhou, A. Pan and S. Liang, *Adv. Funct. Mater.*, 2020, **30**, 2002711.
18 F. Tang, J. Gao, Q. Ruan, X. Wu, X. Wu, T. Zhang, Z. Liu, Y. Xiang, Z. He and X. Wu, *Electrochim. Acta*, 2020, **353**, 136570.
19 Y. Zeng, Y. Wang, Q. Jin, Z. Pei, D. Luan, X. Zhang and X. W. D. Lou, *Angew. Chem., Int. Ed.*, 2021, **60**, 25793–25798.
20 H. Pan, Y. Shao, P. Yan, Y. Cheng, K. S. Han, Z. Nie, C. Wang, J. Yang, X. Li, P. Bhattacharya, K. T. Mueller and J. Liu, *Nat. Energy*, 2016, **1**, 16039.
21 Z. Wang, Z. Ruan, Z. Liu, Y. Wang, Z. Tang, H. Li, M. Zhu, T. F. Hung, J. Liu, Z. Shi and C. Zhi, *J. Mater. Chem. A*, 2018, **6**, 8549–8557.
22 P. Ruan, X. Xu, X. Gao, J. Feng, L. Yu, Y. Cai, X. Gao, W. Shi, F. Wu, W. Liu, X. Zang, F. Ma and X. Cao, *Sustainable Mater. Technol.*, 2021, **28**, e00254.
23 H. Kim, N. Venugopal, J. Yoon and W.-S. Yoon, *J. Alloys Compd.*, 2019, **778**, 37–46.
24 H. Li, L. Jiang, Q. Cheng, Y. He, V. Pavlinek, P. Saha and C. Li, *Electrochim. Acta*, 2015, **164**, 252–259.
25 R. Yang, Z. Guo, L. Cai, R. Zhu, Y. Fan, Y. Zhang, P. Han, W. Zhang, X. Zhu, Q. Zhao, Z. Zhu, C. K. Chan and Z. Zeng, *Small*, 2021, **17**, e2103052.
26 L. Ma, S. Chen, X. Li, A. Chen, B. Dong and C. Zhi, *Angew. Chem., Int. Ed.*, 2020, **59**, 23836–23844.
27 F. Wan, S. Huang, H. Cao and Z. Niu, *ACS Nano*, 2020, **14**, 6752–6760.
28 Z. Yuan, M. Yao, N. Zhang, S. Wang, X. Rui, Q. Zhang and Z. Niu, *Sci. China Mater.*, 2021, **64**, 2182–2192.
29 X. Zhang, S. Wu, S. Deng, W. Wu, Y. Zeng, X. Xia, G. Pan, Y. Tong and X. Lu, *Small Methods*, 2019, **3**, 1900525.
30 Z. Liu, Q. Yang, D. Wang, G. Liang, Y. Zhu, F. Mo, Z. Huang, X. Li, L. Ma, T. Tang, Z. Lu and C. Zhi, *Adv. Energy Mater.*, 2019, **9**, 1902473.
31 H. Li, C. Han, Y. Huang, Y. Huang, M. Zhu, Z. Pei, Q. Xue, Z. Wang, Z. Liu, Z. Tang, Y. Wang, F. Kang, B. Li and C. Zhi, *Energy Environ. Sci.*, 2018, **11**, 941–951.
32 X. Chen, C. Zhong, B. Liu, Z. Liu, X. X. Bi, N. Q. Zhao, X. P. Han, Y. D. Deng, J. Lu and W. B. Hu, *Small*, 2018, **14**, 1702987.
33 Z. Guo, Y. Zhao, Y. Ding, X. Dong, L. Chen, J. Cao, C. Wang, Y. Xia, H. Peng and Y. Wang, *Chem*, 2017, **3**, 348–362.
34 Y. Zhang, Y. Wang, L. Wang, C.-M. Lo, Y. Zhao, Y. Jiao, G. Zheng and H. Peng, *J. Mater. Chem. A*, 2016, **4**, 9002–9008.
35 L. Wang, S. Xie, Z. Wang, F. Liu, Y. Yang, C. Tang, X. Wu, P. Liu, Y. Li, H. Saiyin, S. Zheng, X. Sun, F. Xu, H. Yu and H. Peng, *Nat. Biomed. Eng.*, 2020, **4**, 159–171.

